A Framework for Comparisons of Downburst Precursor Observations using an All-Digital Phased Array Weather Radar

Connor Pearson[1,2] , Tian-You Yu[1,2,3] , David Bodine[1,2] , Sebastian Torres[1,4,5] , Anthony Reinhart[5]

[1] *Advanced Radar Research Center, University of Oklahoma, Norman, Oklahoma*

[2] *School of Meteorology, University of Oklahoma, Norman, Oklahoma*

[3] *School of Electrical and Computer Engineering, University of Oklahoma, Norman, Oklahoma*

[4] *Cooperative Institute for Severe and High-Impact Weather Research and Operations (CIWRO), Norman, Oklahoma*

[5] *National Severe Storms Laboratory, Norman, Oklahoma*

Corresponding author: Connor Pearson, Email: pearson.connor@yahoo.com

Early Online Release: This preliminary version has been accepted for publication in *Journal of Atmospheric and Oceanic Technology*, may be fully cited, and has been assigned DOI 10.1175/JTECH-D-22-0130.1. The final typeset copyedited article will replace the EOR at the above DOI when it is published.

ABSTRACT: Downbursts are a rapidly evolving meteorological phenomena with numerous vertically-oriented precursor signatures, and the temporal resolution and vertical sampling of the current NEXRAD system are too coarse to observe their evolution and precursor signatures properly. A future all-digital polarimetric phased array weather radar (PAR) should be able to improve both temporal resolution and spatial sampling of the atmosphere to provide better observations of rapidly evolving hazards such as downbursts. Previous work has been focused on understanding the trade-offs associated with using various scanning techniques on stationary PAR radars; however, a rotating, polarimetric PAR (RPAR) is a more feasible and cost-effective candidate. Thus, understanding the trade-offs associated with using various scanning techniques on an RPAR is vital in learning how to best observe downbursts with such a system. This work develops a framework for analyzing the trade-offs associated with different scanning strategies in the observation of downbursts and their precursor signatures. A proof-of-concept analysis — which uses a Cloud Model 1 (CM1) simulated downburst-producing thunderstorm — is also performed with both conventional and imaging scanning strategies in an adaptive scanning framework to show the potential value and feasibility of the framework. Preliminary results from the proof-of-concept analysis indicate that there is indeed a limit to the benefits of imaging as an update time speedup method. As imaging is used to achieve larger speedup factors, corresponding data degradation begins to hinder the observations of various precursor signatures.

Accepted for publication in *Journal of Atmospheric and Oceanic Technology.* DOI 10.1175/JTECH-D-22-0130.1.

1. Introduction

A downburst is a localized area of intense downdraft winds with a radar-measured differential velocity across the divergent center greater than 10 m s^{-1} (Fujita 1981; Fujita and Wakimoto 1981; Wilson et al. 1984). Downbursts can impact many areas of human life, from major entertainment events to transportation. Moreover, historically, downbursts have heavily impacted the aviation industry and are responsible for many aviation accidents in the 1970s to early 1980s. After the crash of Delta Airlines flight 191 in Dallas, TX, the Federal Aviation Administration (FAA) quickly began looking for ways to forecast and warn for downbursts, especially in and around airports (Samenow 2013; Smith 2014). Through this previous research, many different precursor signatures observed by radar were identified that warn of an impending downburst at the surface. The precursors include descending reflectivity cores (DRCs), which represent hydrometeor loading (Vasiloff and Howard 2009; Adachi et al. 2016; Kuster et al. 2016); midlevel convergence, which is a mass continuity response to the downdraft (Wakimoto and Bringi 1988; Heinselman et al. 2008; Vasiloff and Howard 2009); differential reflectivity (Z_{DR}) troughs, which represent melting frozen hydrometeors (Scharfenberg 2003; Kuster et al. 2016); specific differential phase (K_{DP}) cores, which represent melting frozen hydrometeors and hydrometeor loading (Kuster et al. 2021); and correlation coefficient (ρ_{hv}) holes, which represent an increasing presence of water coated hailstones (Mahale et al. 2016; Amiot et al. 2019). These precursor signatures generally have a lead time of 4–21 minutes prior to diverging winds at the surface; however, the current Next Generation Weather Radar (NEXRAD) system can provide up to 4 individual full volume coverage pattern (VCP) updates (4.5–7 min each) to observe these signatures. Previous research into a few of these precursor signatures has shown that faster temporal resolutions better capture their evolution and thus, can provide forecasters with additional information when issuing warnings (Newman and Heinselman 2012; Kuster et al. 2016; Adachi et al. 2016; Kuster et al. 2021).

Phased array weather radars (PARs) are capable of producing temporal resolutions small enough to provide rapid updates of quickly evolving meteorological phenomena, such as downbursts, with update times of 30–60 s by electronically steering the beam (Heinselman et al. 2008) or $\approx$ 10 s for systems that support imaging (Isom et al. 2013). Due to the temporal resolution capabilities of a PAR system and needing a cost-effective weather radar solution once the need for multi-function PAR (MPAR) activities dissipated, either a non-rotating or mechanically rotating, planar,

Accepted for publication in *Journal of Atmospheric and Oceanic Technology.* DOI 10.1175/JTECH-D-22-0130.1.

polarimetric PAR (RPAR) appears to be an attractive candidate to replace the NEXRAD system as it can also meet the other weather radar operational requirements for such a replacement system (FAA 2017; Weber et al. 2019). Previous research has investigated how a non-rotating PAR system would operate by looking into data collection from prototype systems such as the National Weather Radar Testbed (NWRT) PAR and the Advanced Technology Demonstrator (ATD) (Zrnic et al. 2007; Torres and Schvartzman 2020; Weber et al. 2020; NSSL 2022); however, with the potential RPAR replacement in mind, Schvartzman et al. (2021) investigated a potential concept of operations associated with an RPAR system. The data from these non-rotating prototype systems have been used in studies for assessing the benefits of rapid-scan PAR (Heinselman et al. 2008; Adachi et al. 2016; Kuster et al. 2016, 2021; Mahre et al. 2020), potential signal processing techniques and benefits (Yu et al. 2007; Kurdzo et al. 2014; Zrnic et al. 2015), radar calibration (Fulton et al. 2016; Schuss et al. 2016; Fulton et al. 2018), and adaptive scanning techniques (Heinselman and Torres 2011; Torres et al. 2014; Torres and Schvartzman 2020). However, there is still a lot of work to determine if PAR technology can meet all current and future needs of the National Weather Service (NWS). Current and future radars such as the ATD (NSSL 2022) and the all-digital polarimetric Horus radar (Palmer et al. 2019; Yeary et al. 2019) look to continue research into the benefits and limitations associated with PAR technology for operational meteorological purposes.

An all-digital polarimetric PAR system, such as Horus, utilizes independent digital transmitters and receivers for each antenna element for each polarization (Palmer et al. 2019). Like other PARs, an all-digital system would be able to utilize various scanning techniques ranging from imaging (Isom et al. 2013; Mahre 2020), beam-multiplexing (Yu et al. 2007), the multiple-beam technique (Melnikov et al. 2015; Zrnic et al. 2015), and even adaptive scanning (Torres and Schvartzman 2020); however, the largest advantage of the all-digital system's independent transmitters and receivers is its maximized scanning flexibility. This scanning flexibility could be exploited to produce better vertical sampling than traditional VCPs in certain situations where gaps in elevation angles are detrimental. For example, by scanning continuously in the vertical (similar to a range-height indicator scan or RHI), vertically oriented changes in thunderstorm structure, associated with downdrafts that precede downbursts, can be captured and tracked through a column (Heinselman et al. 2008; Kuster et al. 2016, 2021). Furthermore, imaging, which transmits a broad (or spoiled) beam and generates multiple individual receiving beams simultaneously through digital beamforming,

Accepted for publication in *Journal of Atmospheric and Oceanic Technology.* DOI 10.1175/JTECH-D-22-0130.1.

has been shown to be a useful update time speedup method (Isom et al. 2013; Kurdzo et al. 2017; Mahre et al. 2020). However, the flexibility associated with the various scanning techniques is not without trade-offs. These trade-offs are seen through degradation in data quality due to higher sidelobe levels in the antenna radiation patterns, beam broadening effects, and loss of sensitivity. Research into the trade-offs associated with these various techniques has been limited in answering questions regarding the importance of data quality versus temporal resolution and how to maximize both. Mahre (2020) and Mahre et al. (2020) looked at this trade-off by examining signatures associated with tornadoes such as tornado debris signatures (TDS) and mesocyclone strength; however, these questions have not been applied to other phenomena, including downbursts.

Previous research has looked into the benefits of rapid-update PAR data for forecaster performance with severe wind and hail events (Bowden 2014; Bowden et al. 2015; Bowden and Heinselman 2016) and the trade-offs associated with using rapid-update PAR data to observe tornadic signatures such as a TDS or mesocyclone strength (Mahre et al. 2020). However, research into downburst observations using rapid-update PAR data is extremely limited, and no previous research has looked into the potential trade-offs associated with utilizing various PAR scanning techniques to observe downbursts nor offered an ideal temporal resolution for downburst observation. This research implements a simulation-based framework to set the groundwork for answering these questions. By utilizing simulations, the framework developed herein allows for direct comparisons of different PAR scanning techniques of the same simulated storm. This allows for a more controlled environment for drawing conclusions on impacts from the various scanning techniques, and the interrogation of various temporal resolutions can be performed to identify temporal resolution requirements for downburst observation.

This work primarily focuses on developing a framework that can be used to assess the trade-offs associated with observations of downbursts and their precursor signatures by various scanning techniques on a rotating all-digital polarimetric PAR. A proof-of-concept analysis of a single simulated wet downburst was performed to showcase the framework's potential in evaluating different scan techniques and focuses on both qualitative and quantitative comparisons between four different scanning strategies. In conjunction with scanning mode selection for downburst observation, the framework developed herein can help show the need of rapid-update radar data for downburst observation. Section 2 details the methodologies used to perform the simulations,

Accepted for publication in *Journal of Atmospheric and Oceanic Technology.* DOI 10.1175/JTECH-D-22-0130.1.

radar emulations, and analysis. Section 3 showcases the results from a proof-of-concept analysis that utilizes the developed framework. Finally, Section 4 summarizes the findings and discusses potential paths for future work.

2. Methods

As previously mentioned, the main goal of this work is to develop a framework for systematically studying how different scanning strategies observe downbursts and their precursor signatures. Figure 1 provides a brief overview of the entire framework along with the flow of variables (Pearson 2022). First, a downburst-producing thunderstorm was generated in a simulation environment. The simulation data was then used to calculate intrinsic polarimetric variables for five hydrometeor types, including mixed-phase precipitation: rain, hail, snow, melting snow, and melting hail. Once the intrinsic polarimetric variables were calculated, the radar emulator Radar Simulator (RSim) was used to produce radar data as observed with a PAR using various scanning strategies. Following the emulations, measurement errors based on estimation processes were calculated and added into the radar data before qualitative and quantitative analyses were performed.

Given that there are no currently operational all-digital polarimetric PARs at the time of this research, the use of simulations allows us to still investigate how such a radar would observe downburst precursor signatures without needing an actual system. Furthermore, using a radar emulator allows for direct comparisons between various scanning strategies as the baseline simulated data and emulation specifications can be held constant for all simulations. However, radar emulators are not without limitations, and the main limitations of RSim include the lack of non-hydrometeor scatterers and not directly relying on radar I/Q data. Without I/Q data, errors of estimates can only be approximately simulated.

a. Simulation

For the analysis that was performed herein, we used a numerical weather prediction (NWP) model. Cloud Model 1 (CM1) version 20.2 was used to generate a downburst-producing thunderstorm over a uniform horizontal grid of 200-by-200 km and a stretched vertical grid from 0-to-20 km above ground level (AGL) (Bryan and Fritsch 2002; Bryan 2020). The stretching in the vertical occurred

Accepted for publication in *Journal of Atmospheric and Oceanic Technology.* DOI 10.1175/JTECH-D-22-0130.1.

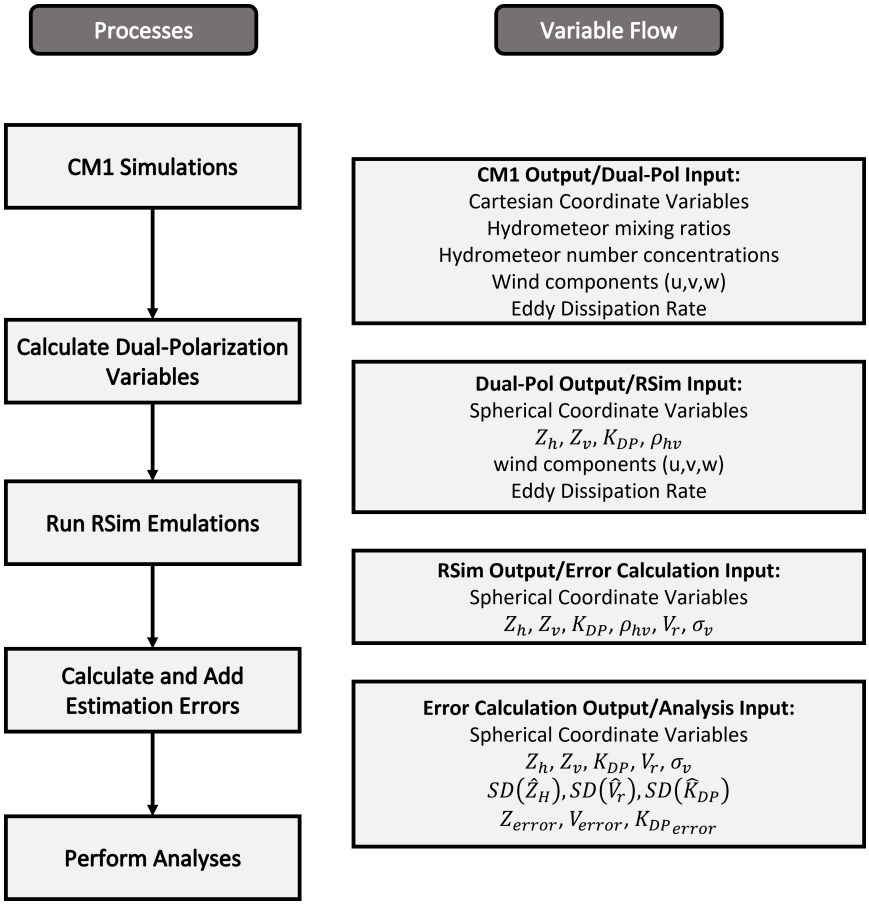

FIG. 1: Simplified flowchart of the framework developed in this work for assessing the performance of various scanning techniques in observing downburst precursor signatures. Figure 2.1 from (Pearson 2022).

from 3 to 9 km with 50-m resolution below 3 km and 550-m resolution above 9 km. The parameterizations used in the CM1 model are listed in Table 1.

To initialize the environmental conditions, an atmospheric sounding was used. The Nashville, TN (KBNA) 16 June 2018 sounding at 0000 UTC was chosen to initialize the model environment (Figure 2). This sounding was associated with a downburst that occurred in the Green Hills area of Nashville, TN (NWS Nashville 2018). Within this environment, convection was initialized using a 5-K warm bubble centered at 1.4-km AGL with a horizontal radius of 10 km and a vertical radius of 1.4 km.

In previous downburst research that utilized simulations, substantial amounts of cooling were added to the downdraft to generate negative buoyancy (Srivastava 1985, 1987; Proctor 1988). This approach works well for studying downburst dynamics within an idealized situation. However, the

Accepted for publication in *Journal of Atmospheric and Oceanic Technology.* DOI 10.1175/JTECH-D-22-0130.1.

TABLE 1: A list of CM1 parameters used in this study.

Parameterization Type	Parameterization Name
Number of Horizontal Grid Points	800
Number of Vertical Grid Points	100
Horizontal Resolution	250 m
Temporal Resolution	10 s
Microphysics Scheme	Morrison Double Moment
Large Ice Category	Hail
Turbulence Scheme	Large-Eddy Simulation (LES)
Small Scale Turbulence Scheme	TKE
Horizontal Boundary Conditions	Radiatively Open
Vertical Boundary Conditions	Free-slip

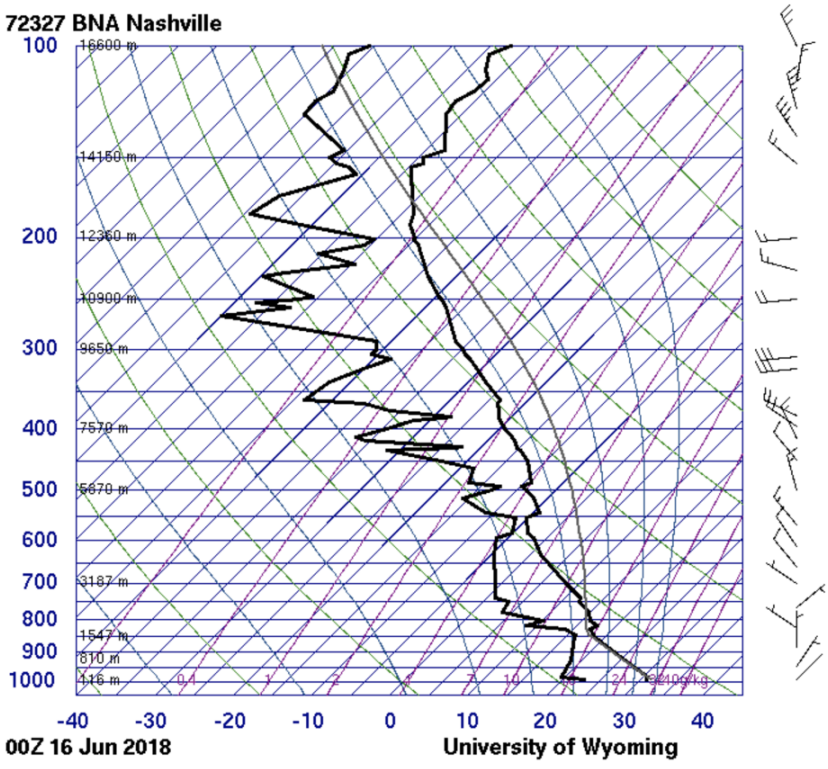

FIG. 2: Sounding from 0000 UTC 16 June 2018 over Nashville, TN (KBNA) associated with a downburst in the Nashville area (University of Wyoming 2021).

goal of this work was to look at precursor signatures associated with microphysical processes in the entire storm environment, and forced cooling would not have produced realistic signatures.

Accepted for publication in *Journal of Atmospheric and Oceanic Technology*. DOI 10.1175/JTECH-D-22-0130.1.

b. RSim

In order to emulate how an all-digital polarimetric PAR would observe the simulated downburst-producing thunderstorm, the radar emulator RSim was used to produce radar data as obtained with the following scanning techniques: pseudo-RHIs from VCP 212, RHIs from the PAR, and imaging with spoiled beams of 2.5°, 5°, and 10° in elevation (Radar Operations Center 2015; Mahre 2020; Mahre et al. 2020). A pseudo-RHI differs from an RHI in that it is generated by piecing together individual elevations angles from a VCP to generate an "RHI" image; however, this new "RHI" image may have significant elevation gaps between the data from consecutive elevation angles. Vertical gaps in the RHI image may be avoided with scanning in an RHI mode, which PAR can naturally support. Within this work, VCP 212 serves as the current operational baseline scanning strategy, RHIs from a PAR are used as an alternative to traditional scanning techniques, and imaging is used as a speedup method available to PARs. These comparisons are performed with the downburst at 30 km range from the radar as the proximity to the radar allows for relatively fine vertical sampling even with 1° sampling.

Within this study, many assumptions were made about the radar architecture and specifications (Table 2). First, it was assumed that the radar was an all-digital polarimetric S-band RPAR with an antenna geometry similar to the Transportable PAR (TPAR) system that was scaled up to the size of a WSR-88D (6-m diameter) (Figure 3) (Palmer et al. 2022). Second, the noise floor was assumed to be the same as that of the WSR-88D radar (-7.5 dBZ at 50 km range). Third, it was assumed that the radar completes a full rotation every 15 s. Finally, all radar emulations were done as part of an adaptive scanning framework.

TABLE 2: Specifications used for all radar emulations performed in RSim.

Specification	Specification Value
Wavelength (m)	0.107
Range Resolution (m)	250
Azimuthal Resolution (°)	1.0
Pulse Repetition Time (ms)	1
Mechanical Rotation Rate (° s^{-1})	24

Within the adaptive scanning framework, the radar was assumed to use additional resources within the allotted rotation rate to make additional RHI scans over an area, or areas, of interest. For

Accepted for publication in *Journal of Atmospheric and Oceanic Technology.* DOI 10.1175/JTECH-D-22-0130.1.

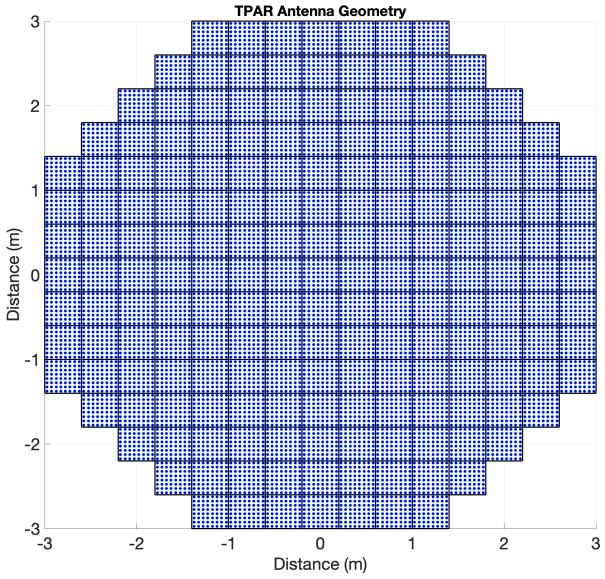

FIG. 3: Antenna geometry of the assumed phased array antenna that is the same as the TPAR antenna from Palmer et al. (2022).

this work, the area of interest was defined as a predetermined 5° sector of azimuth angles, elevation angles up to 20°, and a 5 km swath of ranges centered on 30 km range in order to be centered on the downburst and contain the downburst throughout the analysis time period. The adaptive scanning framework assumed that the total time available to the radar during one mechanical rotation of the antenna could be split into two main parts: T_1 and T_2. T_1 was the time needed for normal radar operations, and T_2 was available for adaptive scanning purposes where $T_1 + T_2 = 15$ s. Using an adaptive scanning framework, the dwell times for each scanning strategy were constant, yet the temporal resolutions for each changed. The limit applied here was that 10° imaging could be performed so quickly, that it could be used to generate RHI scans over the area of interest on every rotation of the radar (i.e., every 15 s). 5° imaging is one-half the spoil factor of 10° imaging, so it would take twice as long to scan the same area; thus, it could only be used to scan the area of interest every two rotations of the radar (i.e., 30 s temporal resolution). This same idea was applied to both the 2.5° imaging and RHI scanning techniques yielding 60 s and 150 s (2.5 min) temporal resolutions, respectively.

RSim reads in single- and polarimetric data along with other variables — u, v, w, and eddy dissipation rate (ε) — that are interpolated to spherical coordinates using the nearest neighbor method to perform the emulations and linearly interpolated in time when necessary (e.g., a scan

Accepted for publication in *Journal of Atmospheric and Oceanic Technology.* DOI 10.1175/JTECH-D-22-0130.1.

time occurs between the 10 s temporal resolution of the simulation data). Once these variables are read in, RSim applies the range weighting function and two-way beam patterns associated with the desired scanning strategy which results in emulated radar observed values of reflectivity factor (Z_h), vertical reflectivity factor (Z_v), K_{DP}, ρ_{hv}, and mean Doppler velocity (V_r). The range weighting function is based on Doviak and Zrnic (1993), and the two-way beam patterns were generated using transmit beam patterns similar to those generated by Schvartzman et al. (2022a,b) with a receive beam pattern generated using a conventional Taylor taper. Finally, RSim calculates additional variables such as spectrum width (σ_v), signal power (S), and Signal-to-Noise Ratio (SNR) before saving all data into an individual file for each update time. The current structure of RSim is a modified version from the one used in Mahre et al. (2020), and the major changes are detailed below.

The first major modification was to allow RSim to "scan" in an RHI mode as opposed to strictly in a PPI mode. This change was made because, as previously mentioned, downburst precursor signatures and the downdrafts associated with downbursts are vertically oriented, and observing their precursor signatures with an RHI scanning strategy would allow for more vertical and temporal continuity in the radar data. Furthermore, with the assumption of an all-digital phased-array antenna, scanning in an RHI mode is much more feasible due to the capability of electronic beam steering compared to a traditional parabolic dish antenna, and the effects of beam broadening are still small with small deviations ($< 10^\circ$) from broadside (Zrnic et al. 2007). Thus, all PAR scanning techniques, RHIs and imaging, were assumed to be generating RHIs. VCP 212, on the other hand, was scanning traditionally in a PPI mode, and the data from all elevation angles at the desired azimuth angle were combined into pseudo-RHIs.

The second major modification was the calculation of polarimetric variables offline to be read into RSim to improve computational efficiency. The intrinsic single- and polarimetric variables — Z_h, Z_v, K_{DP}, and ρ_{hv} — were calculated based on the hydrometeor mixing ratios, unit water content, and mass/volume-weighted diameter (D_m) using polynomial functions of D_m based on T-matrix calculations and empirical functions from Mahale et al. (2019) and Zhang et al. (2021) before being interpolated onto a spherical coordinate system using the nearest-neighbor method. This approach allowed for mixed-phase precipitation influences to be calculated and included in

Accepted for publication in *Journal of Atmospheric and Oceanic Technology.* DOI 10.1175/JTECH-D-22-0130.1.

the data as well. The only modification made to the polarimetric calculation methodology was setting $\alpha = 1$ in the ρ_{hv} calculations compared to $\alpha = 1.5$ from Zhang et al. (2021) for simplicity.

Finally, the last major modification was adjusting the turbulence component of the σ_v calculations to be valid during convection. Previous forms of RSim relied on the Brunt-Vaisala frequency N_{bv}. However, during convection, N_{bv}^2 can be negative, which results in an imaginary N_{bv}. Thus, to avoid using N_{bv}, the new equation for the turbulence component of σ_v was given by equation (10.68) from Doviak and Zrnic (1993):

$$\sigma_t^2 = \left(\frac{r \varepsilon \sigma_\theta A^{1.5}}{0.72} \right)^{2/3} \tag{1}$$

where ε is the eddy dissipation rate and is an output of the CM1 for the entire model domain, r is the range, $A = 1.6$ is a Kolmogorov constant, and σ_θ is the antenna-pattern-induced spectrum width. The antenna pattern induced spectrum width, σ_θ, is given by equation (5.75) from Doviak and Zrnic (1993):

$$\sigma_\theta = \frac{\theta_1}{4\sqrt{\ln(2)}} \tag{2}$$

where θ_1 is the beamwidth assuming a circularly symmetric Gaussian pattern. This is a reasonable assumption for a pencil beam that has a uniform width in both azimuth and elevation. However, for atmospheric imaging situations, θ_1 was calculated such that $\theta_1 = \sqrt{\theta_{el}\theta_{az}}$ where $\theta_{az} = 0.96°$ for all situations and elevation, θ_{el}, varied with spoiled beamwidth and was calculated as the 3-dB beamwidth of the one-way transmit beam.

c. Errors

For the analysis, observation error based on estimation processes was calculated and added into the data to provide more realistic radar data sets for analysis. The quantification of the estimation processes was done using the variances of S and V_r estimators given by Doviak and Zrnic (1993) and Yu et al. (2007):

$$\frac{var(\hat{S})}{S^2} = \frac{1}{M+1} \left[\sum_{l=-M}^{M} \frac{M-|l|+1}{M+1} \rho^2(lT_s) + \frac{N_p^2}{S^2} + 2\frac{N_p}{S} \right] \tag{3}$$

Accepted for publication in *Journal of Atmospheric and Oceanic Technology.* DOI 10.1175/JTECH-D-22-0130.1.

$$var(\hat{V}_r) = \frac{\lambda^2}{32\pi^2 M \rho^2(T_s) T_s^2} \left[(1-\rho^2(T_s)) \sum_{l=-(M-1)}^{M-1} \frac{M-|l|}{M} \rho^2(lT_s) + \frac{N_p^2}{S^2} + 2\frac{N_p}{S}\left[1 - \frac{M-1}{M}\rho(2T_s)\right] \right] \tag{4}$$

where M is the number of pulse pairs, T_s is the pulse repetition time (PRT), ρ is the normalized sample-time autocorrelation function, N_p is the noise power, and $\hat{S}$ and $\hat{v}$ are the estimators for signal power and radial velocity, respectively. S came from the reflectivity factor calculated from the forward operator. The autocorrelation function was the same as what was given by Doviak and Zrnic (1993):

$$\rho(mT_s) = exp\left[-8\left(\frac{\pi\sigma_v m T_s}{\lambda}\right)^2\right], \text{where} \quad m = 0, 1, 2, ...(M_p - 1) \tag{5}$$

where λ is the radar wavelength and M_p is the number of pulses.

The standard deviation of radial velocity was calculated by taking the square root of the variance. However, in order to obtain the standard deviation of the reflectivity factor in dB units, the following equation from Mahre (2020) was used:

$$SD(\hat{Z}_h) = 10\log_{10}\left(1 + \frac{SD(\hat{S})}{S}\right). \tag{6}$$

The standard deviation for K_{DP} was calculated using equations from Melnikov (2004):

$$SD(\hat{\Phi}_{dp}) = \frac{1}{\sqrt{2}\,\rho_{hv}}\left(\frac{SNR_h + SNR_v + 1}{M\,SNR_h\,SNR_v} + \frac{1-\rho_{hv}}{M_I}\right)^{1/2} \quad \text{(rad)} \tag{7}$$

and

$$SD(\hat{K}_{dp}) = \frac{SD(\hat{\Phi}_{dp})}{\sqrt{2}\,L} \tag{8}$$

where M_I is the number of independent pulse pairs, L is the measurement resolution, SNR_h (from here on SNR) is the signal-to-noise ratio in the horizontal polarization, SNR_v is the signal-to-noise ratio in the vertical polarization, and ρ_{hv} is the correlation coefficient. SNR and SNR_v are related by $SNR = Z_{DR}\,SNR_v$.

Accepted for publication in *Journal of Atmospheric and Oceanic Technology.* DOI 10.1175/JTECH-D-22-0130.1.

It was assumed that errors were normally distributed with a mean of zero and with standard deviations equal to $SD(\hat{Z}_h)$, $SD(\hat{V}_r)$, and $SD(\hat{K}_{dp})$. This value was then added onto the existing idealized data to generate more realistic data sets, and all analyses were performed using these new data sets.

d. Proof-of-Concept Analysis

The proof-of-concept analysis focused on both qualitative and quantitative comparisons regarding each scanning strategy's ability to observe and detect a downburst and its precursor signatures. The precursor signatures that were analyzed are:

- intensity, size, and evolution of K_{DP} cores (Kuster et al. 2021);
- intensity, size and evolution of DRCs (Isaminger 1988; Roberts and Wilson 1989; Kuster et al. 2016);
- intensity of mid-level convergence around 4-km AGL (Vasiloff and Howard 2009; Kuster et al. 2016).

For qualitative comparisons, only one set of errors was used, and comparisons occurred at 30-km range along one azimuth angle through the area of interest.

In addition, the quantitative analysis involved using different metrics related to the size, shape, and intensity of the precursor signatures over the area of interest, centered on the downburst, involving five contiguous azimuth angles, elevation angles up to 20°, and a 5-km swath in range, centered at 30-km range. For the DRC and K_{DP} core, these metrics included the 95^{th} percentile K_{DP} and Z_h values (intensity), the total volume of elevated Z_h ($\geq$ 55 dBZ) and K_{DP} ($\geq 2.0^\circ$ km^{-1}) (size), and the heights of the top and bottom of the Z_h column and K_{DP} core (size) (Isaminger 1988; Heinselman et al. 2008; Amiot et al. 2019; Kuster et al. 2021). The evolution was further quantified for the intensity of the DRC and K_{DP} core by calculating the rate of change in the 95^{th} percentile values of Z_h and K_{DP} over the area of interest as a measure of each signature's intensification. For the V_r signatures (surface divergence and midlevel convergence), the maximum (minimum) radial ΔV was calculated to denote divergence (convergence), and the maximum (minimum) value from the five azimuth angles was kept to denote the peak intensity of the divergence (convergence) signature (Isaminger 1988; Eilts 1987). The area of surface divergence was also quantified as

Accepted for publication in *Journal of Atmospheric and Oceanic Technology.* DOI 10.1175/JTECH-D-22-0130.1.

the total number of range gates associated with a divergent radial $\Delta V \geq 10$ m s^{-1}, and then the number of range gates was converted to an area using the size of a range gate at 30-km range. The metrics were calculated from the average of 10 different error-analysis data sets. Thus, unlike the qualitative analysis, they do not represent the observations of just one error-analysis case but rather represent the average metrics for all error analysis cases within the proof-of-concept analysis.

In order to determine when the downburst was in contact with the surface, a combination of the surface divergence and area of surface divergence was used to split the analysis time period ($t = 34$ min to $t = 57$ min) into pre-, mid-, and post-downburst time periods based on the model data. The pre-downburst time period is the time period before the downburst reaches the surface (times prior to $t = 46$ min), the mid-downburst time period is the time period when the downburst is in contact with the "surface" (based on the data from the 0.5° elevation angle) ($t = 46$ min to $t = 50$ min), and the post-downburst time period is the time period after the downburst ΔV threshold is no longer met (times after $t = 50$ min). These distinctions are important because the point of a precursor signature is to warn of an impending downburst, and the evolution of the precursor signatures was analyzed as either before, during, or after the downburst reached the surface.

In order to quantify the performance of each scanning strategy, the root-mean-squared error (RMSE) was calculated using the equation from Mackey (1998):

$$RMSE = \left[\sum_{i=1}^{P} \frac{(x_f - x_o)^2}{P} \right]^{0.5} \tag{9}$$

where P is the number of samples over the analysis time period ($t = 34$ min to $t = 57$ min), which varied with scanning strategy; x_f is the metric estimate from the model radar data; and x_o is the metric estimate from each scanning strategy radar data, which was calculated from the average of 10 separate estimation error data sets.

3. Results

The results presented here only apply to a single wet downburst case; however, they can still show the potential value of the simulation framework and how it can be utilized moving forward.

While only one range is presented here, an investigation at 90 km range was done in a thesis associated with this work (Pearson 2022). Although Pearson (2022) uses a slightly different

Accepted for publication in *Journal of Atmospheric and Oceanic Technology.* DOI 10.1175/JTECH-D-22-0130.1.

methodology to calculate the dual-polarization variables, differences between the results at 30 km range were minimal and the conclusions were ultimately the same.

a. Downburst Reflectivity Evolution

Before diving into comparisons between the various scanning strategies, it is important to orient oneself with the downburst. Figure 4 shows the evolution of the model Z_h interpolated onto a spherical grid along multiple azimuth angles in the area of interest from $t = 39$ min (Fig. 4a) to $t = 53$ min (Fig. 4o) at 1-min resolution. Multiple azimuth angles were used to show the DRC evolution from a DRC-centric point of view as the downburst moves across multiple azimuth angles during the time period of interest. The time period from $t = 39$ min to $t = 53$ min was chosen as it includes the evolution of the DRC through the pre-, mid-, and post-downburst times periods.

In Figure 4a ($t = 39$ min), the origins of a DRC are beginning to form with an area of elevated Z_h (≥ 55 dBZ) at 3–6 km AGL and around 30-km range. By the next minute (Fig. 4b), the DRC has intensified with values ≥ 70 dBZ and suggests increased hydrometeor loading from hail. It is noted that ≥ 70 dBZ Z_h returns are likely unrealistically high according to previous research of wet downbursts from Eilts (1987) and Wakimoto and Bringi (1988); however, Newman and Heinselman (2012) observed a downburst producing thunderstorm over central Oklahoma that produced maximum reflectivities up to 74 dBZ, which indicates that the observations are plausible albeit unlikely to occur in the real atmosphere. Nevertheless, the storm maintains the ≥ 70 dBZ signature for another seven minutes before the maximum value in the core of the DRC drops to $\geq$ 65 dBZ in Fig. 4j ($t = 48$ min). In Fig. 4i–l, the DRC combines with another strong Z_h signature that has moved into the area forming a cohesive DRC that stretches from the surface to $\approx$ 5-km AGL with two Z_h maxima. The upper maximum is associated with the hydrometeor loading seen in Fig. 4b–h while the lower maximum moved into the area with the storm motion after the DRC reached the surface. As the DRC reached and maintained contact with the surface, the lower maximum moved down range, and the upper maximum was able to be tracked toward the surface indicating the continued descent of the lofted hydrometeors associated with the hydrometeor loading seen in Fig. 4b–h. By $t = 50$ min (Fig. 4l), the hydrometeor loading has reached the surface and had begun to dissipate, and this dissipation can be tracked through the near total disappearance of the ≥ 60 dBZ values in the elevated Z_h region (≥ 55 dBZ) by Fig. 4o ($t = 53$ min).

Accepted for publication in *Journal of Atmospheric and Oceanic Technology.* DOI 10.1175/JTECH-D-22-0130.1.

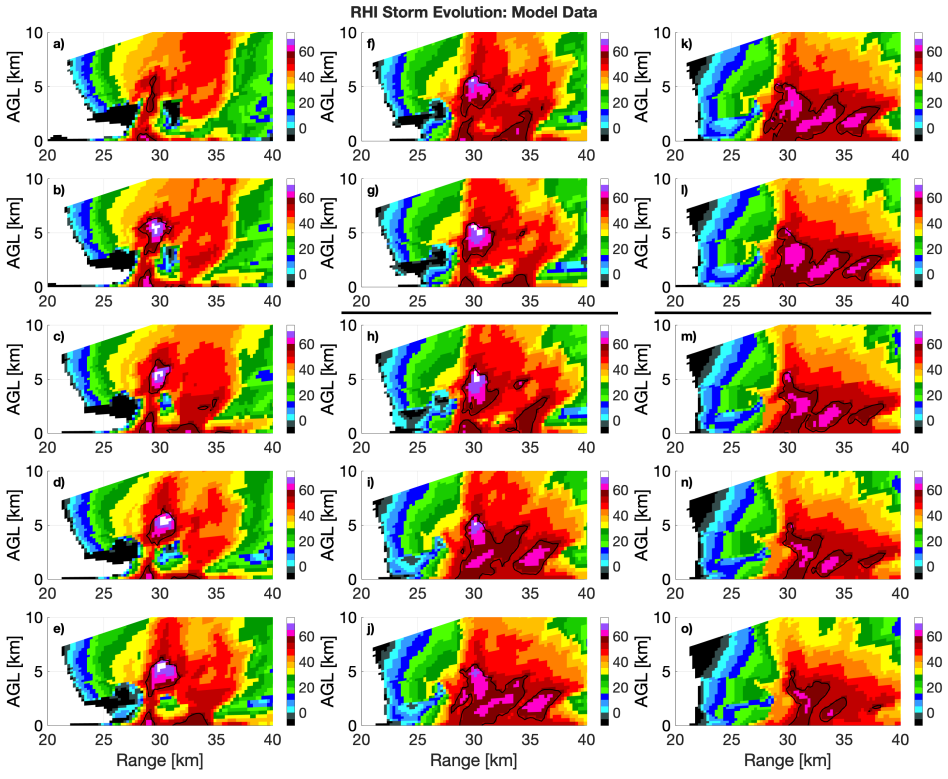

FIG. 4: RHI Images of model Z_h interpolated onto a spherical grid along multiple azimuth angles, to take a DRC-centric view, at 1-min temporal resolution from $t = 39$ min (panel a) to $t = 53$ min (panel o). The black contours represent the 55-dBZ level used to denote the area of the Z_h column. The horizontal black lines before panel h and after panel l denote the start and end of the downburst at the surface, respectively.

b. Qualitative Analysis

The qualitative analysis focused on observations involving midlevel convergence, surface divergence, a DRC, and a K_{DP} core. The observations were located roughly 30 km away from the radar along azimuth 174°, which cuts through the eastern side of the downburst during the analysis period, with vertical sampling from 0.5° to 20° elevation. The downburst primarily descends along azimuth angle 174; however, it does deviate off of azimuth 174 during the analysis time period, but comparisons at a single time period are not impacted by this movement as the various scanning strategies are seeing the same part of the storm at each specific time. The qualitative analysis directly compared the idealized model data with the RHI scanning and imaging using 2.5°, 5°, and 10° spoiling on transmit (including errors of estimates). All qualitative figures have the 55-dBZ Z_h contour plotted in black to show the boundaries of the DRC.

Accepted for publication in *Journal of Atmospheric and Oceanic Technology.* DOI 10.1175/JTECH-D-22-0130.1.

Figure 5 showcases V_r at two separate times ($t = 42$ min and $t = 47$ min) for comparison. The V_r is the weighted average of the radial velocity profile, and the weights in azimuth, elevation, and range are dominated by the reflectivity and the two-way antenna pattern. Starting with $t = 42$ min, Figure 5a.1–a.5 show RHI images along azimuth 174° through the east side of the area of interest, and there are two main areas of comparisons. The first location is the layer 3–5 km AGL between 27.5- and 32.5-km range, and the second is the layer 0–2 km AGL between 30- and 32.5-km range. The layer 3–5 km AGL and 27.5–32.5-km range is the region associated with a midlevel convergence signature. When looking at the model data (Fig. 5a.1), the midlevel convergence (black arrow) is located in the middle of the Z_h column (black contour). When comparing the midlevel convergence signature as the spoiling factor increases (black arrows, Fig. 5a.2–a.5), the midlevel convergence signature becomes more difficult to visually observe with increasing spoil factor. This is likely caused by greater vertical sidelobe contamination increasing as the spoil factor increases, which leads to strong gradients in V_r becoming smeared. It is unlikely that the issue is due to wider mainlobes associated with imaging as there is only a small difference in vertical mainlobe beamwidth (6-dB) among all the imaging cases (Table 3).

TABLE 3: Two-way 6-dB beamwidths associated with each scanning strategy's transmit beam pattern coupled with the central (0° offset) receive beam.

Beam Pattern	-6 dB BW Azimuth	-6 dB BW Elevation
Pencil	1.01°	1.01°
2.5° Spoil	0.94°	1.52°
5° Spoil	0.92°	1.52°
10° Spoil	0.94°	1.49°

In the layer 0–2 km AGL, an area of strong outbound V_r is seen between 30- and 32.5-km range in the model data (red arrow, Fig. 5a.1). This region is best observed by the RHI (Fig. 5a.2) and 2.5° imaging (Fig. 5a.3) scanning strategies. It is still visible in the 5° imaging (Fig. 5a.4); however, the positive Doppler velocities of the signature decrease in the 10° imaging data (Fig. 5a.5), which is again caused by vertical sidelobe contamination effects.

Examining the signature 5-min later in Fig. 5b.1–b.5 ($t = 47$ min), this time corresponds to the early stages of the downburst at the surface. This is evident just inside the 30-km range in the model data (black arrow, Fig. 5b.1). This divergent V_r signature is best represented by the RHI image (black arrow, Fig. 5b.2) as the structure and intensity is similar to what is seen in the

Accepted for publication in *Journal of Atmospheric and Oceanic Technology.* DOI 10.1175/JTECH-D-22-0130.1.

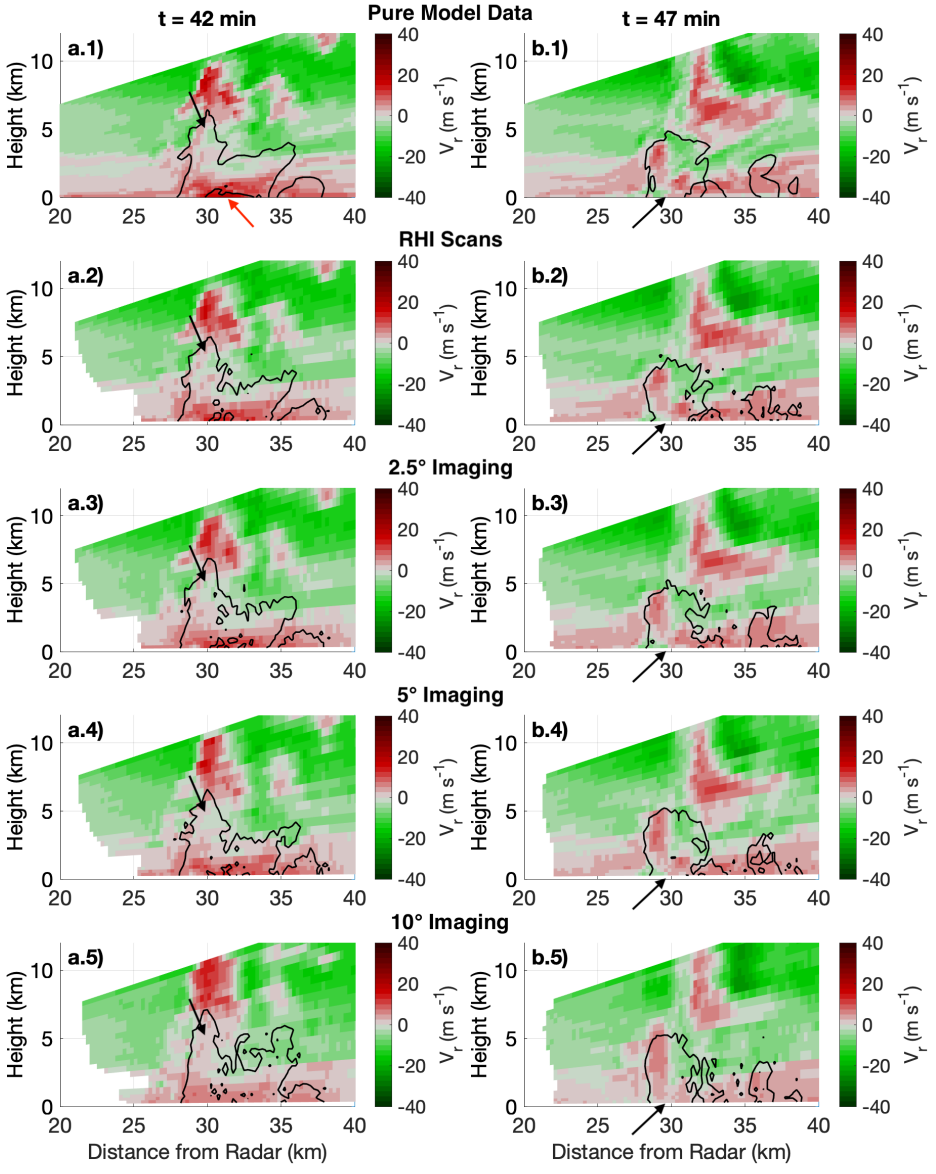

FIG. 5: RHI scans of V_r along azimuth angle 174° at $t = 42$ min and $t = 47$ min which cuts through the eastern part of the downburst. Black contours represent the 55-dBZ level used to denote the area of the Z_h column. Panels a.1 and b.1 represent the pure model data, panels a.2 and b.2 the RHI scans, panels a.3 and b.3 imaging at 2.5°, panels a.4 and b.4 imaging at 5°, and panels a.5 and b.5 imaging at 10°. In panels a.1–a.5, the black arrows show the location of the midlevel convergence signature, and the red arrow shows the location of the strong outbound V_r signature. In panels b.1–b.5, the black arrows show the location of the surface divergence signature.

Accepted for publication in *Journal of Atmospheric and Oceanic Technology*. DOI 10.1175/JTECH-D-22-0130.1.

model data (Fig. 5b.1) with minor differences likely due to sampling differences. The 2.5° and 5° imaging (black arrows, Fig. 5b.3–b.4) have similar divergence signatures to the RHI image (Fig. 5b.2). However, the divergence signature is difficult to discern in the 10° imaging in the location seen in Fig. 5b.1–b.4 with only positive Doppler velocities. Moreover, 10° imaging has noticeably weaker outbound V_r values in the lowest 2 km between 30 and 35 km range compared to the other scanning strategies (Fig. 5b.1–b.5). This lack of definition throughout the lowest 2 km is likely caused by sidelobe contamination as was seen in Fig. 5a.1–a.5.

The hypothesis that sidelobe contamination is causing poor velocity signature detection is further examined in Fig. 6 by exploring the distributions of Z_h and the two-way antenna beam patterns. It can be seen in Fig. 6a that the positive outbound V_r are in the lowest 1 km with decreasing V_r with height while the strongest Z_h are around 5-km AGL and are generally 15-dBZ larger than those associated with the lowest 1 km. When looking at the individual beam patterns, the 5° imaging beam pattern has -40 dB sidelobes up to about 2.5 km where the difference in reflectivities over the layer is roughly 5 dBZ; however, the 10° imaging beam pattern has -40 dB sidelobes up to just below 5-km AGL where the difference in reflectivities over the layer is ≈15 dBZ. Thus, the ≥ -40 dB sidelobes is likely influencing the lowest V_r signatures for 10° imaging whereas the sidelobe contamination is lower for imaging with smaller spoil factors and non-existent for the RHI (pencil beam) scanning strategy (Fig. 6c).

Next, the impact of different antenna radiation patterns associated with different scanning techniques on the DRC is explored. When looking at Z_h at $t = 42$ min (Fig. 7a.1–a.5), the DRC is prominent around 30-km range between 1- and 5-km AGL. Within the DRC, the model data shows reflectivities reaching ≥ 70 dBZ around 5-km AGL at 30-km range. The core of the DRC (≥ 60 dBZ Z_h) stretches from 29–30.5-km range and 0–6-km AGL with Z_h decreasing to around 30-dBZ by 10-km AGL. The elevated Z_h region (≥ 55 dBZ) stretches past 35-km range with another ≥ 60 dBZ region visible between 34–35-km range and 1–3-km AGL.

The RHI data (Fig. 7a.2) has the same general structure and intensity seen in the model data with a core of Z_h reaching ≥ 65 dBZ around 5-km AGL, and Z_h decreases above the DRC to about 30-dBZ by 10-km AGL. Furthermore, the ≥ 55-dBZ region has a similar shape to the model data with the DRC on the left of the region, the ≥ 55-dBZ Z_h region generally below 3-km AGL, and the pointed tip just outside of 35-km range. The 2.5° imaging data (Fig. 7a.3) is very similar to the

Accepted for publication in *Journal of Atmospheric and Oceanic Technology.* DOI 10.1175/JTECH-D-22-0130.1.

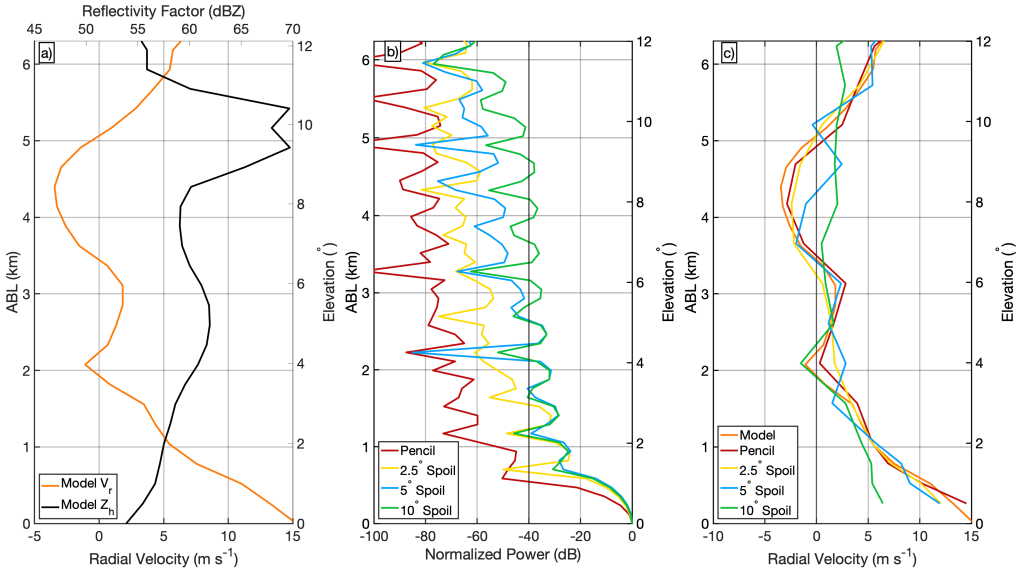

FIG. 6: a) Vertical profile of model Z_h and V_r over the lowest 12 elevation angles along azimuth 174° at 30 km range at $t = 42$ min which cuts through the eastern part of the downburst. b) Beam patterns for pencil beam (red), 2.5° imaging (yellow), 5° imaging (blue), and 10° imaging (green) for a beam located at 0.5° elevation. c) Vertical profile of model and emulated V_r for each scanning strategy: RHI (red), 2.5° imaging (yellow), 5° imaging (blue), and 10° imaging (green).

RHI image (Fig. 7a.2) when looking at the DRC structure and intensity. The 5° imaging data (Fig. 7a.4) begins to show some noticeable differences in the DRC. In addition to spreading the gradients, the impact of imaging on data quality is evident with the noisier data. Furthermore, although not directly impacting the downburst observations, the ≥ 60-dBZ region around 34–35-km range is much smaller, and the pointed tip is less resolved compared to the model, RHI, and 2.5° imaging data. Finally, and as expected, the 10° imaging data (Fig. 7a.5) is the most different from what was seen in the model data (Fig. 7a.1). The DRC appears to stretch higher than the previous scanning strategies, and the Z_h above the DRC only decreases to about 40-dBZ at 10-km AGL.

The differences seen in the 10° imaging are likely caused by sidelobe-contamination effects. These effects are common with imaging as the larger the spoil factor, the further away from the mainlobe ≥ -40 dB sidelobes can extend (as seen in Figure 6b). For 10° imaging, this is seen in Figure 8a which shows a vertical profile of Z_h from 0.5–10-km AGL (0.5° to 20° elevation) at 29.75-km range. In Figure 8a, it is evident that there is some smearing of reflectivity with the 10° imaging as ≥ 55 dBZ stretches to 7-km AGL compared to ≈ 6-km AGL in the other scanning strategies and the model data. Furthermore, it can be seen that these impacts were noted up to

Accepted for publication in *Journal of Atmospheric and Oceanic Technology*. DOI 10.1175/JTECH-D-22-0130.1.

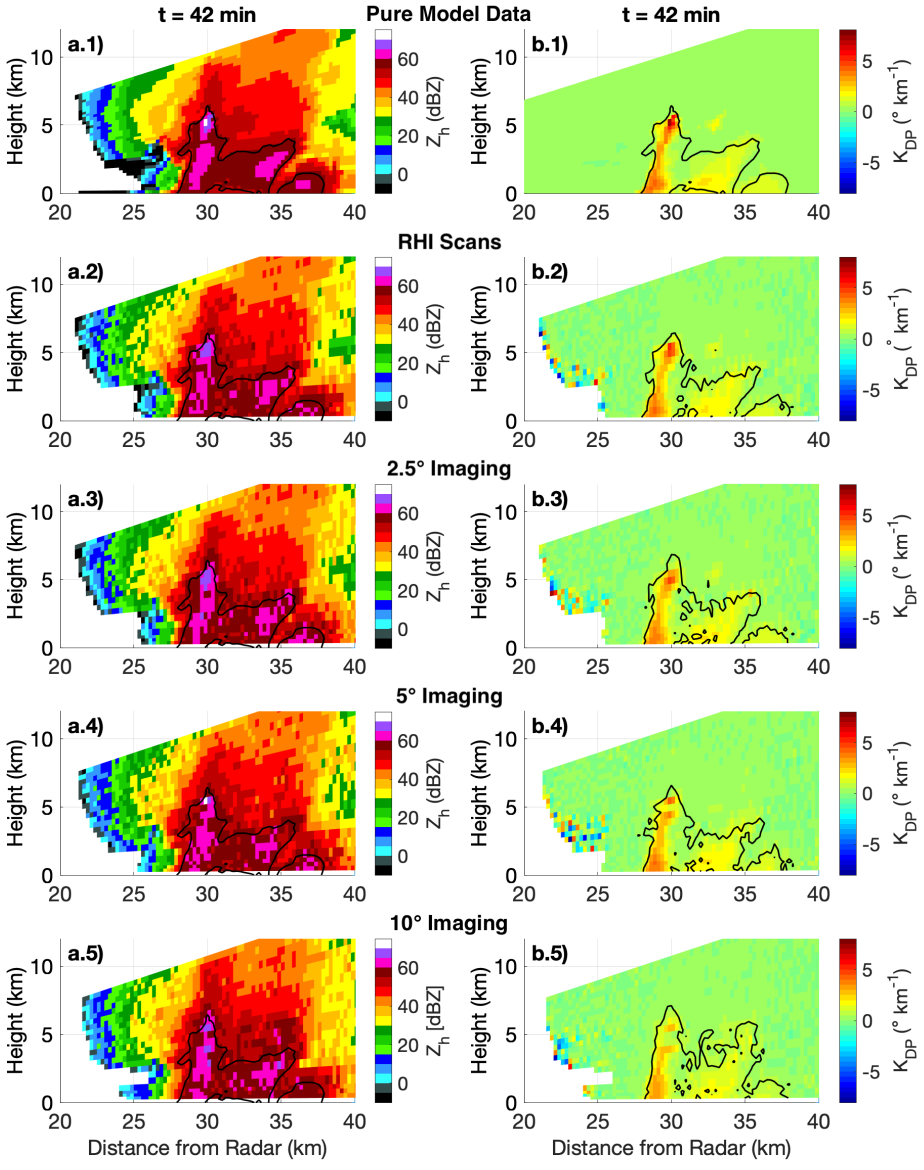

FIG. 7: RHI scans of Z_h (panels a.1 – a.5) and K_{DP} (panels b.1 – b.5) along azimuth angle 174° at $t = 42$ min which cuts through the eastern part of the downburst. Scanning strategies are the same as in Figure 5. Black contours in panels a.1–a.5 represent the 55-dBZ level used to denote the area of the model Z_h core, while black contours in panels b.1–b.5 represent the 55-dBZ level used to denote the area of the Z_h core for each scanning strategy.

10-km AGL as the 10° imaging shows a Z_h value of about 45-dBZ while the other scanning strategies are much lower (Fig. 8a).

Accepted for publication in *Journal of Atmospheric and Oceanic Technology.* DOI 10.1175/JTECH-D-22-0130.1.

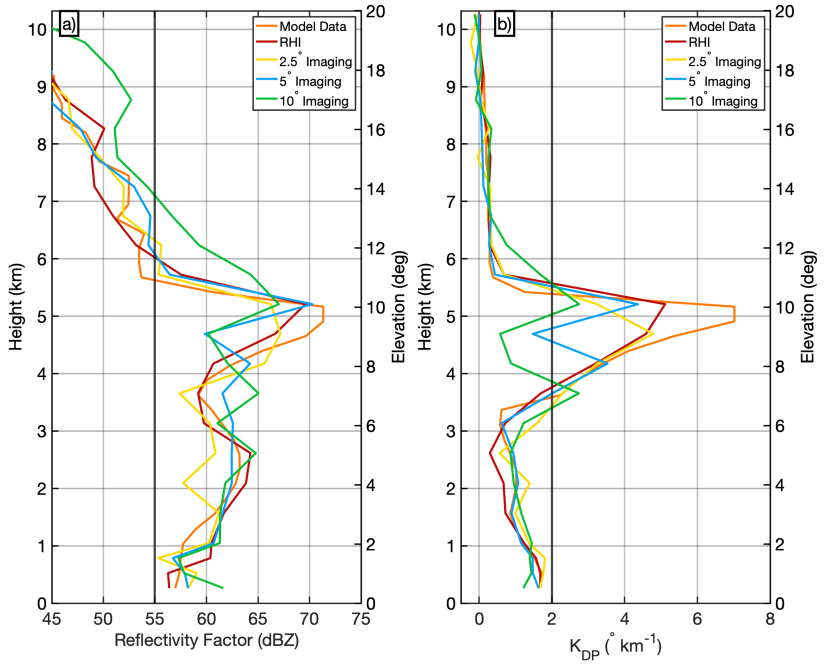

FIG. 8: a) Vertical profile of Z_h over every elevation angle along azimuth 174° at 29.75km range at $t = 42$ min for model data and all scanning strategies. b) Same as a) but for K_{DP}.

The final precursor signature explored is the K_{DP} core. In Figure 7, the K_{DP} core ($\geq 2°$ km^{-1}) in the model data (Fig. 7b.1) stretches from the surface up to about 5-km AGL, which corresponds to the environmental melting layer in the simulations. Furthermore, the maximum K_{DP} value is located around 5-km AGL with a value of $\approx 7°$ km^{-1} (Fig. 8b). When looking at the RHI image (Fig. 7b.2), the general structure and intensity of the K_{DP} core are similar to the model data (Fig. 7b.1), albeit the maximum value is lower and more diffuse. The differences between Fig. 7b.2 and Fig. 7b.1 are likely caused by sampling differences as the RHI has 1° sampling spacing above 2° elevation and the model data has a uniform 0.5° spacing. The 2.5° imaging (Fig. 7b.3) is similar to Fig. 7b.2 (RHI) with no apparent major differences. At 5° imaging (Fig. 7b.4), the top of the K_{DP} core becomes harder to observe and is actually split in two (see Fig. 8b where the 5° imaging profile drops below the K_{DP} core threshold just below 5-km AGL). Furthermore, the maximum value is suppressed in this region with values barely reaching 4° km^{-1} (Fig. 8b). For 10° imaging (Fig. 7b.5), the issues seen at 5° imaging are more pronounced with a larger spatial separation in the bottom and top portions of the K_{DP} core, and the maximum value is suppressed even more to about 2.5° km^{-1} (Fig. 8b). These effects in the 5° and 10° imaging are likely caused by sidelobe

Accepted for publication in *Journal of Atmospheric and Oceanic Technology*. DOI 10.1175/JTECH-D-22-0130.1.

contamination averaging down the K_{DP} signature in the upper regions of the K_{DP} core as both the 5° and 10° imaging have the largest number of ≥ -40-dB sidelobes which can stretch 2.5-km and 5-km away vertically from a given range gate, respectively (Fig. 6b).

c. Quantitative Analysis

As previously mentioned, the quantitative analysis focuses on various metrics to measure the size, shape, and intensity of the downburst and its precursor signatures. The metrics analyzed below include surface divergence, area of surface divergence, midlevel convergence, total volume of the DRC and K_{DP} core, the 95^{th} percentile Z_h and K_{DP} and rate of change of the 95^{th} percentile Z_h and K_{DP}. These metrics, and the qualitative analysis as a whole, showcases how rapidly the various parameters used to measure downbursts can change, which further indicates the need for faster update times that PARs can provide. All plots showcase the temporal resolution of the data by plotting only the last known data point available at any given time. Each PAR scanning mode (RHI, 2.5° imaging, 5° imaging, and 10° imaging) has a different temporal resolution, and this analysis takes into account these temporal resolution differences as well as the data quality differences.

As mentioned in Section 2.d, the surface divergence and area of surface divergence — shown in Figure 9 — were used to determine the timing of the downburst at the surface to split the analysis time period into pre-, mid-, and post-downburst time periods based on the model data (vertical black lines on Figures 9–13).

When looking at Figure 9a, which shows the mean of 10 different error realizations, finding the downburst is slightly difficult as the maximum radial ΔV is at or above the downburst definition of ≥ 10 m s^{-1} throughout the analysis period. This "noisy" maximum radial ΔV is due to the fact that the area of interest is located at the edge of a single-cellular thunderstorm and interactions between the environmental winds and the storm's outflow winds are causing divergent signatures to be observed outside the downburst of interest. Thus, coupling the maximum ΔV with the area of the ΔV ≥ 10 m s^{-1} helped distinguish when the downburst occurred (Fig. 9b). Using Figure 9a–b, the time period between t = 46 min and t = 50 min was determined to be the mid-downburst time period, timing of the downburst at the surface, as there is a relative maximum in both the maximum radial ΔV and the area of surface divergence. Thus, as mentioned in Section 2.d, times prior to t = 46 min are referred to the pre-downburst time period, and times after t = 50 min are referred

Accepted for publication in *Journal of Atmospheric and Oceanic Technology.* DOI 10.1175/JTECH-D-22-0130.1.

to the post-downburst time period. The relative maxima in both surface divergence and area of surface divergence in the mid-downburst time period are seen in all scanning strategies except for 10° imaging. After $t = 46$ min, the 10° imaging deviates from all other scanning strategies and actually has a maximum ΔV that drops below the 10 m s^{-1} threshold, which in turn results in the area of surface divergence going to zero. This indicates that the 10° imaging did not produce radar data that allowed for the detection of the downburst at the surface as the criteria were not met. This is caused by sidelobe-contamination effects similar to what was seen in the qualitative analysis (Section 3b) when the radar data from the 10° imaging was insufficient to properly resolve the V_r signatures in the lowest 2 km.

With the other scanning strategies detecting a downburst, the 2.5-min temporal resolution of the RHI is not small enough to resolve some of the features seen in the model data (shown at 30 s temporal resolution). However, as seen in Table 4, the radar data obtained with RHI recorded the second lowest RMSE values for surface divergence and area of surface divergence equal to 4.02 m s^{-1} and 8.17 km^2, respectively. The model evolution of both the surface divergence (Fig. 9a) and area of surface divergence (Fig. 9b) is most accurately depicted in the 60-s temporal resolution of the 2.5° imaging with the best RMSEs of 3.05 m s^{-1} and 6.67 km^2, respectively (Table 4). The 30-s temporal resolution of the 5° imaging provided faster updates compared to the 2.5° imaging and RHI scanning strategies, and the RMSEs of the radar data obtained with 5° imaging were similar to those associated with the radar data obtained with the RHI at 4.65 m s^{-1} for the surface divergence and 8.51 km^2 for the area of surface divergence (Table 4). The worst performing scanning strategy according to the RMSEs was the 10° imaging, which produced data that was hindered by sidelobe contamination effects, and had RMSEs equal to 7.27 m s^{-1} and 10.27 km^2, respectively (Table 4). The quantitative analysis for surface divergence and area of surface divergence has similar findings to the qualitative analysis (Section 3b). However, incorporating realistic scan times and errors illustrates that 2.5° imaging best optimizes scan time and data quality.

The first precursor signature analyzed is midlevel convergence that was calculated as the maximum radial ΔV over the 5 azimuth angles of interest on the elevation angle closest to 4-km AGL. In Figure 10, the left vertical black line at $t = 46$ min represents the pre-downburst time period, and thus, this area represents the precursor time period. From the start of the analysis, the midlevel convergence steadily increases from at or below 5 m s^{-1} to over 20 m s^{-1} for all scanning strategies

Accepted for publication in *Journal of Atmospheric and Oceanic Technology.* DOI 10.1175/JTECH-D-22-0130.1.

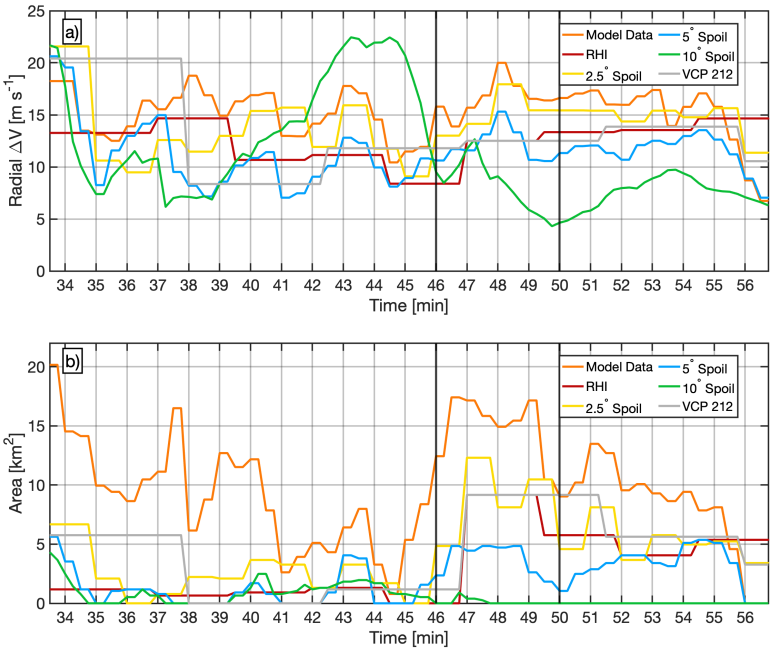

FIG. 9: a) Surface ΔV (divergence) and b) area of surface divergence with $\Delta V \geq 10$ m s^{-1}. The temporal resolutions for each scanning strategy are as follows: 4.5 min for VCP 212, 2.5 min for RHI, 1 min for 2.5° imaging, 30 s for 5° imaging, and 15 s for 10° imaging. The left vertical black line at $t = 46$ min represents the start of the downburst, and the right vertical black line at $t = 50$ min represents the end of the downburst at the surface.

TABLE 4: RMSE values for each PAR scanning strategy associated with each metric. Bold values denote the worst performing scanning strategy for each metric.

Metric	RHI	2.5° Imaging	5° Imaging	10° Imaging
Surface Divergence (m s^{-1})	4.02	3.05	4.65	**7.27**
Area of Surface Divergence (km^2)	8.17	6.67	8.51	**10.27**
Midlevel Convergence (m s^{-1})	4.07	4.34	3.99	**5.01**
DRC Volume (km^3)	10.56	23.37	22.52	**26.83**
K_{DP} Core Volume (km^3)	5.49	**11.33**	10.16	9.15
ΔZ_h (dBZ min^{-1})	**1.37**	1.12	0.78	0.90
ΔK_{DP} (° km^{-1} min^{-1})	**0.22**	0.19	0.11	0.15

except for 10° imaging. This maximum has general agreement — within ≈1 min — between the model data, RHI, 2.5° imaging, and 5° imaging while the maximum in the data from 10° imaging is delayed by about 2-min. The timing of this maximum agrees with results from Isaminger (1988), and the fact that midlevel convergence had a larger magnitude than the surface divergence is not unrealistic based on previous research (Eilts 1987).

Accepted for publication in *Journal of Atmospheric and Oceanic Technology*. DOI 10.1175/JTECH-D-22-0130.1.

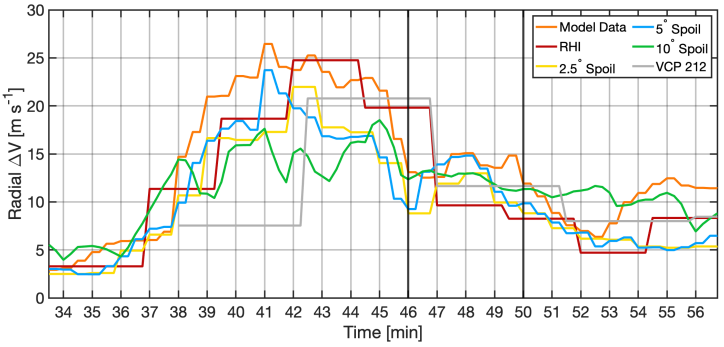

FIG. 10: Midlevel convergence at elevation angle closest to 4 km AGL. The left vertical black line at $t = 46$ min represents the start of the downburst, and the right vertical black line at $t = 50$ min represents the end of the downburst at the surface.

The agreement in the maximum midlevel convergence is generally irrespective of temporal resolution with the 2.5-min (RHI), 60-s (2.5° imaging), and 30-s (5° imaging) resolutions having maxima within about 1 min of one another; however, the finer evolution of the midlevel convergence is lost in the RHI data (at 2.5-min resolution) even though the RHI has the second lowest RMSE of 4.07 m s^{-1} (Table 4). The 60-s resolution of 2.5° imaging does fairly well with tracking the evolution of the signature with an RMSE of 4.34 m s^{-1}, but the radar data from the 5° imaging follows the evolution shown in the model data the best with an RMSE of 3.99 m s^{-1} (Table 4). 10° imaging, with an RMSE of 5.01 m s^{-1}, is adversely impacted by sidelobe contamination — similar to what was seen in the qualitative data at $t = 42$ min in Figure 5a.5 — as the influences from a larger resolution volume should also have impacted observations at 2.5° and 5° imaging (Table 4). When compared to a traditional NEXRAD scanning strategy — with a 4.5-min temporal resolution — the mid-level convergence viewed in the data from the model, 2.5° imaging, and 5° imaging increase from 10 m s^{-1} to $\geq$ 20 m s^{-1} in less than one traditional VCP update (4.5-min) ($t = 37$ min to $t = 41$ min) (VCP 212 in Fig. 10). The ability to observe this rapid intensification at 60-s or 30-s resolution provides additional observations, increased continuity of observations, and thus, more "lead time" for an operational forecaster over slower scanning techniques such as the RHI and VCP 212. This increased continuity can in turn help boost forecaster confidence that midlevel convergence is actually intensifying and that a downburst is more likely to occur.

Moving onto quantification of the DRC and K_{DP} core, the first metric discussed is the volume of each signature. Figure 11a shows the total volume of the DRC throughout the analysis period

Accepted for publication in *Journal of Atmospheric and Oceanic Technology*. DOI 10.1175/JTECH-D-22-0130.1.

while Fig. 11b shows the same for the K_{DP} core. In both panels, once the individual signature was detected — passing a 10 continuous range-gate threshold — the volume of each signature grows to a maximum before dissipating by the end of the analysis period. In Fig. 11a and 11b, the volume of both the DRC and K_{DP} core increase to a maximum just as the downburst ends at the surface before the signature started decreasing in size. Therefore, the maximum volume of the DRC or K_{DP} core cannot even be classified as a precursor signature for this case since the maximum value occurs after the downburst reached the surface. When looking at both the DRC and K_{DP} core, the evolution of the volumes might be a better precursor signature as there is a noticeable increase in the DRC and K_{DP} core volumes before the downburst reached the surface. However, the evolution of the volumes is not well captured at the coarse temporal resolution associated with the RHI scanning strategy — as evidenced by the RHI radar data having the highest and second highest RMSE values for the DRC volume and K_{DP} Core volume (Table 4). However, with the finer temporal resolutions, $\leq$ 60 s, there is general agreement between the evolution of the volumes of these signatures.

It can be observed that using the radar data from all scanning strategies results in an overestimation of the volume compared to using the model data for both the DRC and K_{DP} core (Figure 11). This is likely caused by differences of resolution volume sizes between model data and emulated data as the model data has 0.5° resolution in elevation while the emulated data has 1.0° (RHI) or 1.5° (imaging) resolution in elevation (Table 3). Thus, with a uniform 1° sample spacing for the PAR scanning strategies (RHI and imaging), the resolution volumes for the radar data from imaging were overlapping throughout most of the RHI, which resulted in several atmospheric volumes being counted twice. Thus, it is not surprising that signature volumes measured from the radar data from imaging were acutely overestimated. However, the radar data from the RHI did not experience this drastic overestimation as the 6-dB beamwidth for the two-way beam pattern was 1.01° in both the azimuth and elevation directions, which helped limit overlapping volumes (Table 4).

Forecasters are often interested in whether or not a trend in a radar signature is persisting as well as the magnitude of the change. Thus, a possible benefit of PARs is their finer temporal resolutions allow for more accurate computation of rates of change in radar signatures. To explore this, the final quantitative metrics discussed are the 95^{th} percentile of Z_h and K_{DP} and the rate of 95^{th} percentile change in time for Z_h and K_{DP} over the area of interest (Figure 12 and 13). The 95^{th}

Accepted for publication in *Journal of Atmospheric and Oceanic Technology.* DOI 10.1175/JTECH-D-22-0130.1.

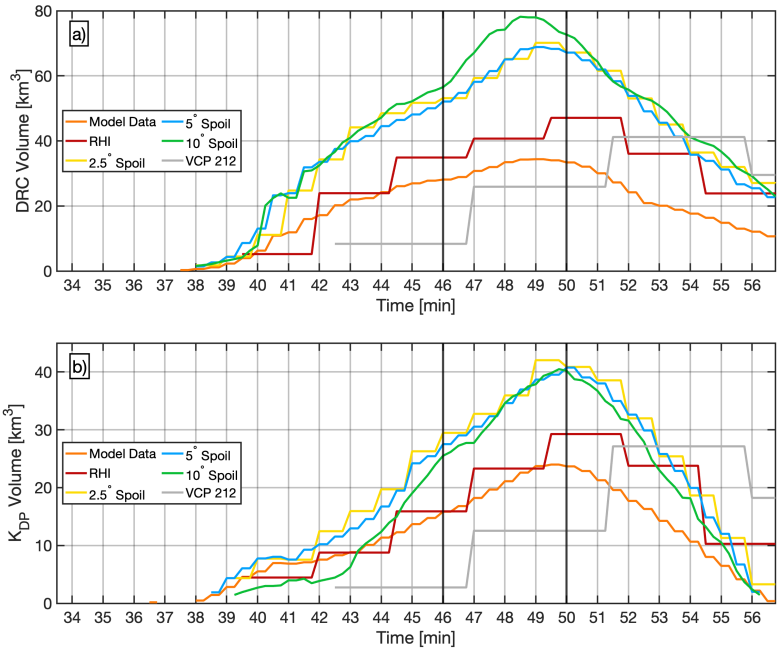

FIG. 11: a) Total volume of the DRC column throughout the analysis period for model data and all scanning strategies. b) Same as panel a but for the K_{DP} core. Volume calculation assumed all range gates were the size of a range gate at 30 km range. The left vertical black line at $t = 46$ min represents the start of the downburst, and the right vertical black line at $t = 50$ min represents the end of the downburst at the surface.

percentile value was used to denote the intensity of the DRC and K_{DP} core; however, the rate of 95^{th} percentile change in time was used to determine how rapidly the precursor signatures intensified. When looking at Figure 12, there is a noticeable increase in both the 95^{th} percentile Z_h and K_{DP} values starting approximately 7–8 minutes before the downburst reaches the surface. However, exploiting the PAR's finer temporal resolution, calculating the rate of 95^{th} percentile change in both Z_h (Fig. 13a) and K_{DP} (Fig. 13b) indicates a rapid intensification of the 95^{th} percentile Z_h and K_{DP} values around $t = 39$ min. This shows that, about 7 min prior to the downburst reaching the surface, the DRC and K_{DP} core were rapidly intensifying with rates of intensification of ≥ 4 dBZ min^{-1} and $\geq 0.5°$ km^{-1} min^{-1} for all scanning strategies except for the RHI and VCP 212. The reason that the radar data from the RHI and VCP 212 did not resolve the major increase is that the rate of change decreases at coarser temporal resolutions. The intensification of the storm could be a sign that the storm was more likely to produce a downburst, and using a similar metric to the one used in Isaminger (1988), the radar data from all scanning strategies with temporal resolutions

Accepted for publication in *Journal of Atmospheric and Oceanic Technology*. DOI 10.1175/JTECH-D-22-0130.1.

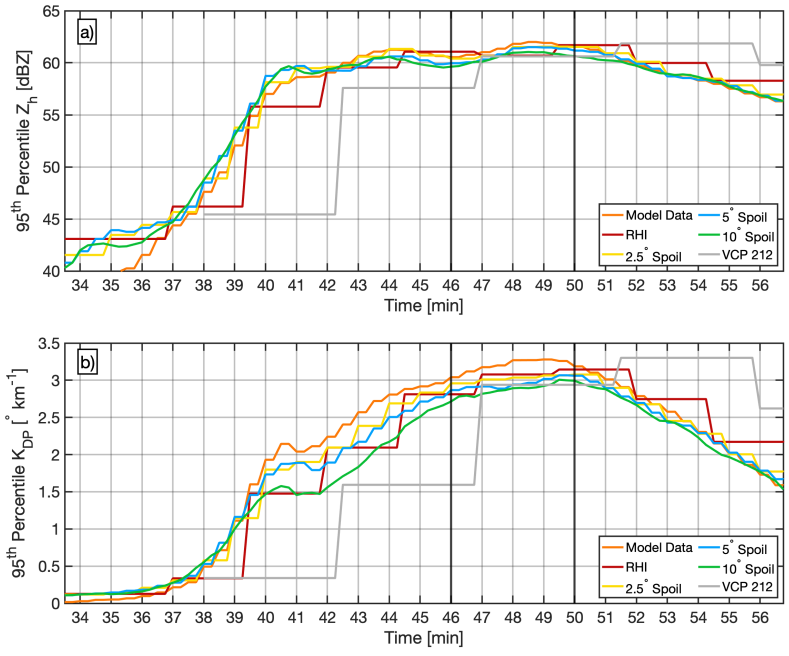

FIG. 12: a) 95^{th} percentile Z_h over the analysis period. b) Same as panel a but for K_{DP}. The left vertical black line at $t = 46$ min represents the start of the downburst, and the right vertical black line at $t = 50$ min represents the end of the downburst at the surface.

≤ 60 s had a 95^{th} percentile Z_h reach 54 dBZ and remained there for at least 3 consecutive scans over the area of interest before the wind shear reached the surface (Fig. 12a).

4. Conclusions

In this study, a framework was developed to analyze the benefits and trade-offs associated with conventional and various PAR scanning techniques in the observation of downburst precursor signatures such as midlevel convergence, DRCs, and K_{DP} cores. After generating a downburst-producing thunderstorm in a simulation environment, radar emulations were performed to produce radar data as would be obtained from a pseudo-RHI from VCP 212 along with four different scanning techniques that would be feasible with an all-digital polarimetric PAR (RHI and 2.5°, 5°, and 10° imaging). The temporal resolutions for each PAR scanning strategy varied such that larger spoil factors lead to smaller scan times. Errors of estimates were added to the data to provide more realistic radar data sets to support more meaningful qualitative and quantitative analyses. The qualitative analysis focused on direct comparisons between radar data from each

Accepted for publication in *Journal of Atmospheric and Oceanic Technology*. DOI 10.1175/JTECH-D-22-0130.1.

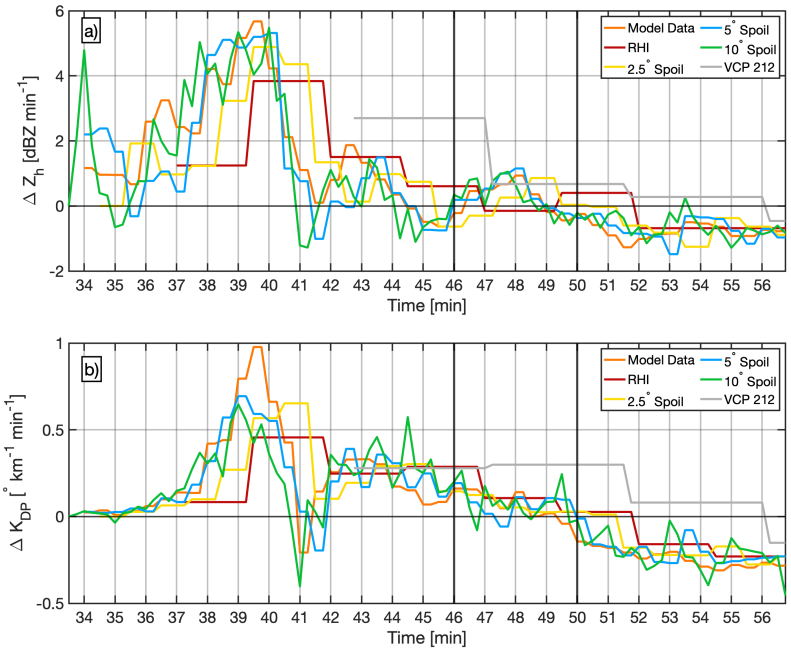

FIG. 13: a) Rate of 95^{th} percentile change in time for Z_h over the analysis period. b) Same as panel a but for K_{DP}. The left vertical black line at $t = 46$ min represents the start of the downburst, and the right vertical black line at $t = 50$ min represents the end of the downburst at the surface. The horizontal black line represents the zero line or no rate of 95^{th} percentile change in time.

scanning strategy to visually compare the size, shape, and intensity of the precursor signatures to one another. Statistical quantitative analysis focused on comparisons of various metrics used to quantify the size, shape, and intensity of the precursor signatures analyzed herein.

The framework developed was showcased through a proof-of-concept analysis, which served as a first look into the utility and potential value of the framework and informed how this framework could be used in the future. Furthermore, the impacts of PAR scanning strategies based on imaging on polarimetric radar variables were systematically explored. However, the results from the proof-of-concept analysis are limited as they only involved analysis of a single wet downburst case. Although these results cannot yet be generalized, the findings gathered from the proof-of-concept analysis are still insightful with two main takeaways for this case:

- Temporal resolutions of at least 60 s better track the evolution of precursor signatures by providing more accurate maximum values, earlier observations of key features, and more continuity between observations.

Accepted for publication in *Journal of Atmospheric and Oceanic Technology*. DOI 10.1175/JTECH-D-22-0130.1.

- There was no additional benefit below 30 s temporal resolution when using imaging as a speedup method due to data degradation from sidelobe contamination. The sidelobe contamination started to noticeably occur when using 5° imaging. However, the data degradation greatly hindered the collection of accurate observations with 10° imaging, most notably seen in the surface divergence signature and with 10° imaging being generally associated with the highest RMSE values.

- With larger spoil factors, noticeable reductions in precursor signature maximums were observed (specifically in K_{DP}; Fig. 8 and Fig. 12), and these reductions could lead to underestimation of storm strength and hinder a forecaster's confidence in the likelihood of a storm to produce a downburst.

The above conclusions relating to utilizing imaging as a speedup method do have some similarities to those from Mahre et al. (2020). Namely, when spoiling in a direction of strong Z_h gradients, data degradation of the Doppler velocities occurs and worsens with increasing spoil factor. However, the degree of data degradation in the Doppler velocities appeared more impactful here on downburst detection and strength compared to impacts observed for mesocyclone intensity. This is seen with data degradation greatly hindering accurate observations at 10° for a downburst to the point where the downburst was not detectable while observations of mesocyclone intensity only marginally decreased in Mahre et al. (2020). It is hypothesized that the differences in observed impacts are related to the intensity of the gradient of Z_h for a given signature. That is to say, the larger the Z_h gradient, the greater the possible impact of data degradation from larger spoil factors. Mahre et al. (2020) examined how horizontal gradients of Z_h impacted observations of mesocyclone strength, while this study investigated how vertical gradients of Z_h impacted downburst intensity. Thus, this difference indicates the need to study different phenomena to fully understand how these trade-offs change depending on the meteorological case observed.

There are many possibilities for future work. First, generalizing the results from the proof-of-concept analysis would be vital before any broad recommendations could be made. With this generalization, it would also be advantageous to investigate many different dry and wet downburst simulations in varying environmental conditions to take into account a wider range of possibilities, how well downburst can be observed with various scanning strategies at different ranges from the radar (e.g., 60 km, 90 km, etc.), and how various scanning rates impact the performance of different

Accepted for publication in *Journal of Atmospheric and Oceanic Technology.* DOI 10.1175/JTECH-D-22-0130.1.

scanning strategies. The simulation framework can be applied to almost any weather phenomenon that CM1 can simulate such as supercells, hurricanes, convective initiation, etc., so it can be used for a wide range of PAR application studies. Second, further modification of the radar emulator would be ideal to allow for analysis of other scanning techniques that can also be used as speedup methods such as beam-multiplexing (Yu et al. 2007) or the multiple-beam technique (Melnikov et al. 2015; Zrnic et al. 2015). Ultimately, this framework could help lead to the development of a downburst detection algorithm or be used to help determine when adaptive scanning would be advantageous for downburst detection.

Accepted for publication in *Journal of Atmospheric and Oceanic Technology.* DOI 10.1175/JTECH-D-22-0130.1.

Acknowledgments. Funding for this research was provided under NOAA-University of Oklahoma Cooperative Agreement NA210AR4320204 (CIWRO). David Bodine is also supported by NSF grant AGS-2114817. The authors specifically thank Dr. David Schvartzman for providing the necessary antenna beam patterns and Samuel Emmerson for many helpful suggestions throughout this research.

Data availability statement. Owing to the large size of the numerical simulations, the CM1 model and radar simulation data generated for this project are available by contacting the authors. The radar simulation software and namelists to reproduce the CM1 simulations will be provided upon requests.

References

Adachi, T., K. Kusunoki, S. Yoshida, K.-I. Arai, and T. Ushio, 2016: High-speed volumetric observation of a wet microburst using x-band phased array weather radar in Japan. *Mon. Wea. Rev.*, **144 (10)**, 3749–3765.

Amiot, C. G., L. D. Carey, W. P. Roeder, T. M. McNamara, and R. J. Blakeslee, 2019: C-band dual-polarization radar signatures of wet downbursts around Cape Canaveral, Florida. *Wea. Forecasting*, **34**, 103–131.

Bowden, K. A., 2014: The phased array radar innovative sensing experiment 2013. M.S. thesis, School of Meteorology, The University of Oklahoma.

Bowden, K. A., and P. L. Heinselman, 2016: A qualitative analysis of NWS forecasters' use of phased-array radar data during severe hail and wind events. *Wea. Forecasting*, **31**, 43–55.

Bowden, K. A., P. L. Heinselman, D. M. Kingfield, and R. P. Thomas, 2015: Impacts of phased-array radar data on forecaster performance during severe hail and wind events. *Wea. Forecasting*, **30**, 389–404.

Bryan, G. H., 2020: CM1 homepage. National Center for Atmospheric Research and National Science Foundation, URL https://www2.mmm.ucar.edu/people/bryan/cm1/.

Bryan, G. H., and J. M. Fritsch, 2002: A benchmark simulation for moist nonhydrostatic numerical models. *Mon. Wea. Rev.*, **130**, 2917–2928.

Accepted for publication in *Journal of Atmospheric and Oceanic Technology.* DOI 10.1175/JTECH-D-22-0130.1.

Doviak, R. J., and D. S. Zrnic, 1993: *Doppler Radar and Weather Observations*. Dover Publications, Inc.

Eilts, M. D., 1987: Low-altitude wind shear detection with doppler radar. Tech. rep., National Severe Storms Laboratory.

FAA, 2017: Spectrum efficient national surveilance radar program (sensr) - formal request for information (rfi). Tech. rep., Federal Aviation Administration. URL https://faaco.faa.gov/index.cfm/attachment/download/73825.

Fujita, T. T., 1981: Tornadoes and downbursts in the context of generalized planetary scales. *J. Atmos. Sci.*, **38**, 1511–1534.

Fujita, T. T., and R. Wakimoto, 1981: Five scales of airflow associated with a series of downbursts on 16 July 1980. *Mon. Wea. Rev.*, **109**, 1438–1456.

Fulton, C., J. Salazar, D. Zrnic, D. Mirkovic, I. Ivic, and D. Doviak, 2018: Polarimetric phased array calibration for large-scale multi-mission radar applications. *2018 IEEE Radar Conference*, IEEE.

Fulton, C., M. Yeary, D. Thompson, J. Lake, and A. Mitchell, 2016: Digital phased arrays: Challenges and opportunities. *Proceedings of the IEEE*, **104**, 487–503.

Heinselman, P. L., D. L. Priegnitz, K. L. Manross, T. M. Smith, and R. W. Adams, 2008: Rapid sampling of severe storms by the national weather radar testbed phased array radar. *Wea. Forecasting*, **23**, 808–824.

Heinselman, P. L., and S. M. Torres, 2011: High-temporal-resolution capabilities of the national weather radar testbed phased-array radar. *J. Appl. Meteor. Climatol.*, **50**, 579–593.

Isaminger, M. A., 1988: A preliminary study of precursors to Huntsville microbursts. Tech. rep., Lincoln Laboratory. URL https://www.ll.mit.edu/r-d/publications/preliminary-study-precursors-huntsville-microbursts.

Isom, B., and Coauthors, 2013: The atmospheric imaging radar: Simultaneous volumetric observations using a phased array weather radar. *J. Atmos. Oceanic Technol.*, **30**, 655–675.

Accepted for publication in *Journal of Atmospheric and Oceanic Technology.* DOI 10.1175/JTECH-D-22-0130.1.

Kurdzo, J. M., B. L. Cheong, R. D. Palmer, G. Zhang, and J. B. Meier, 2014: A pulse compression waveform for improved-sensitivity weather radar observations. *J. Atmos. Oceanic Technol.*, **31**, 2713–2731.

Kurdzo, J. M., and Coauthors, 2017: Observations of severe local storms and tornadoes with the atmospheric imaging radar. *Bull. Amer. Meteor. Soc.*, **98**, 915–935.

Kuster, C. M., B. R. Bowers, J. T. Carlin, T. J. Schuur, J. W. Brogden, R. Toomey, and A. Dean, 2021: Using K_{DP} cores as a downburst precursor signature. *Wea. Forecasting*, **36**, 1183–1198.

Kuster, C. M., P. L. Heinselman, and T. J. Schuur, 2016: Rapid-update radar observations of downbursts occurring within an intense multicell thunderstorm on 14 June 2011. *Wea. Forecasting*, **31 (3)**, 827–851.

Mackey, J. B., 1998: Forecasting wet microbursts associated with summertime airmass thunderstorms over the southeastern United States. M.S. thesis, Graduate School of Engineering, Air Force Institute of Technology.

Mahale, V. N., G. Zhang, and M. Xue, 2016: Characterization of the 14 June 2011 Norman, Oklahoma, downburst through dual-polarization radar observations and hydrometeor classification. *J. Appl. Meteor. Climatol.*, **55**, 2635–2655.

Mahale, V. N., G. Zhang, M. Xue, J. Gao, and H. D. Reeves, 2019: Variational retrieval of rain microphysics and related parameters from polarimetric radar data with a parameterized operator. *J. Atmos. Oceanic Technol.*, **36**, 2483–2500.

Mahre, A., T. Yu, and D. J. Bodine, 2020: A comparison of scan speedup strategies and their effect on rapid-scan weather radar data quality. *J. Atmos. Oceanic Technol.*, **37**, 1955–1972.

Mahre, W. A., 2020: Quantitative analysis of rapid-scan phased array weather radar benefits and data quality under various scan conditions. Ph.D. thesis, University of Oklahoma.

Melnikov, V. M., 2004: Simultaneous transmission mode for the polarimetric WSR-88D: *Statistical Biases and Standard Deviations of Polarimetric Variables*. Tech. rep., National Severe Storms Laboratory, Norman, OK.

Accepted for publication in *Journal of Atmospheric and Oceanic Technology.* DOI 10.1175/JTECH-D-22-0130.1.

Melnikov, V. M., R. J. Doviak, and D. S. Zrnic, 2015: A method to increase the scanning rate of phased-array weather radar. *IEEE Transactions on Geoscience and Remote Sensing*, **53**, 5634–5643.

Newman, J. F., and P. L. Heinselman, 2012: Evolution of a quasi-linear convective system sampled by phased array radar. *Mon. Wea. Rev.*, **140**, 3467–3486.

NSSL, 2022: Research tools: Advanced Technology Demonstrator. NOAA National Severe Storms Laboratory, URL https://www.nssl.noaa.gov/tools/radar/atd/.

NWS Nashville, 2018: Twitter, URL https://twitter.com/NWSNashville/status/1008214282406891522.

Palmer, R. D., C. J. Fulton, J. Salazar, H. Sigmarsson, and M. Yeary, 2019: The "Horus" radar - an all-digital polarimetric phased array radar for multi-mission surveillance. *35th Conference on Environmental Information Processing Technologies*, Amer. Meteor. Soc., Phoenix, AZ.

Palmer, R. D., and Coauthors, 2022: Transportable phased array radar: Meeting weather community needs. *38th Conference on Environmental Information Processing Technologies*, Amer. Meteor. Soc., Houston, TX.

Pearson, C., 2022: Assessing scanning strategies with all-digital phased array weather radars for characterization and detection of microbursts. M.S. thesis, College of Atmospheric and Geographic Sciences, University of Oklahoma.

Proctor, F., 1988: Numerical simulations of an isolated microburst. part i: Dynamics and structure. *J. Atmos. Sci.*, **45**, 3137–3160.

Radar Operations Center, 2015: WSR-88D volume coverage pattern (VCP) improvement initiatives. URL https://www.roc.noaa.gov/WSR88D/PublicDocs/NewTechnology/New_VCP_Paradigm_Public_Oct_2015.pdf.

Roberts, R. D., and J. W. Wilson, 1989: A proposed microburst nowcasting procedure using single-doppler radar. *J. Appl. Meteor.*, **28**, 285–303.

Samenow, J., 2013: Ronald Reagan's near brush with weather-induced death: the August 1, 1983 microburst. *Washington Post*.

Accepted for publication in *Journal of Atmospheric and Oceanic Technology.* DOI 10.1175/JTECH-D-22-0130.1.

Scharfenberg, K., 2003: Polarimetric radar signatures in microburst-producing thunderstorms. *31st International Conference on Radar Meteorology*, Amer. Meteor. Soc.

Schuss, J., T. Sikina, J. Hilliard, P. Makridakis, J. Upton, J. Yeh, and S. Sparagna, 2016: Large scale phased array calibration. *2016 IEEE International Symposium on Phased Array Systems and Technology (PSAT)*, IEEE.

Schvartzman, D., J. D. D. Diaz, J. L. Salazar-Cerreno, T. Yu, R. D. Palmer, and M. S. McCord, 2022a: A hybrid antenna pattern synthesis method for the polarimetric atmospheric imaging radar (PAIR). *2022 IEEE Radar Conference*.

Schvartzman, D., R. Palmer, T. Yu, R. Reinke, and F. Nai, 2022b: A pattern synthesis method for polarimetric weather observations with the all-digital Horus phased array radar. *38th Conference on Environmental Information Processing Technologies*, Amer. Meteor. Soc.

Schvartzman, D., S. M. Torres, and T.-Y. Yu, 2021: Distributed beams: Concept of operations for polarimetric rotating phased array radar. *IEEE Transactions on Geoscience and Remote Sensing*, **59 (11)**, 9173–9191, https://doi.org/10.1109/TGRS.2020.3047090.

Smith, M., 2014: Defeating the downburst: 20 years since the last U.S. commercial jet accident from wind shear. *Washington Post*.

Srivastava, R., 1985: A simple model of evaporatively driven downdraft: Application to microburst downdraft. *J. Atmos. Sci.*, **42**, 1004–1023.

Srivastava, R., 1987: A model of intense downdrafts driven by melting and evaporation of precipitation. *J. Atmos. Sci.*, **44**, 1752–1773.

Torres, S., and Coauthors, 2014: A demonstration of adaptive weather-surveillance capabilities on the national weather radar testbed phased-array radar. *2014 International Radar Conference*, IEEE.

Torres, S. M., and D. Schvartzman, 2020: A simulation framework to support the design and evaluation of adaptive scanning for phased-array weather radars. *J. Atmos. Oceanic Technol.*, **37**, 2321–2339.

Accepted for publication in *Journal of Atmospheric and Oceanic Technology.* DOI 10.1175/JTECH-D-22-0130.1.

University of Wyoming, 2021: University of Wyoming, College of Engineering, Department of Atmospheric Sciences, URL http://weather.uwyo.edu/upperair/sounding.html.

Vasiloff, S., and K. Howard, 2009: Investigation of a severe downburst storm near Phoenix, Arizona, as seen by a mobile doppler radar and the KIWA WSR-88D. *Wea. Forecasting*, **24**, 856–867.

Wakimoto, R., and V. Bringi, 1988: Dual-polarization observations of microbursts associated with intense convection: The 20 July storm during the MIST project. *Mon. Wea. Rev.*, **116**, 1521–1539.

Weber, M., V. Melnikov, D. Zrnic, K. Hondl, R. R. Zellner, and B. Hudson, 2020: Experimental validation of the multibeam technique for rapid-scan, meteorological phased-array radar. Amer. Meteor. Soc., *36th Conference on Environmental Information Processing Techniques*.

Weber, M. E., J. Pica, C. D. Curtis, I. R. Ivic, D. Conway, and J. Y. N. Cho, 2019: Panel discussion: The next-generation operational weather radar network. *Phased Array Radar Symposium*, Phoenix, AZ, Amer. Meteor. Soc.

Wilson, J. W., R. D. Roberts, C. Kessinger, and J. McCarthy, 1984: Microburst wind structure and evaluation of doppler radar for airport wind shear detection. *J. Appl. Meteor. Climatol.*, **23 (6)**, 898–915.

Yeary, M., R. Palmer, C. Fulton, J. Salazar, and H. Sigmarsson, 2019: Recent advances on an s-band all-digital mobile phased array radar. *2019 IEEE International Symposium on Phased Array System & Technology (PAST)*.

Yu, T., M. B. Orescanin, C. D. Curtis, D. S. Zrnic, and D. E. Forsyth, 2007: Beam multiplexing using the phased-array weather radar. *J. Atmos. Oceanic Technol.*, **24**, 616–626.

Zhang, G., J. Gao, and M. Du, 2021: Parameterized forward operators for simulation and assimilation of polarimetrie radar data with numerical weather predictions. *Adv. Atmos. Sci.*, **38**, 737–754.

Zrnic, D. S., V. M. Melnikov, R. J. Doviak, and R. Palmer, 2015: Scanning strategy for the multifunction phased-array radar to satisfy aviation and meteorological needs. *IEEE Geoscience and Remote Sensing Letters*, **12**, 1204–1208.

Accepted for publication in *Journal of Atmospheric and Oceanic Technology*. DOI 10.1175/JTECH-D-22-0130.1.

Zrnic, D. S., and Coauthors, 2007: Agile-beam phased array radar for weather observations. *Bull. Amer. Meteor. Soc.*, **88**, 1753–1766.

Accepted for publication in *Journal of Atmospheric and Oceanic Technology.* DOI 10.1175/JTECH-D-22-0130.1.